



Deposited via The University of Leeds.

White Rose Research Online URL for this paper:

<https://eprints.whiterose.ac.uk/id/eprint/145175/>

Version: Accepted Version

Article:

McCutcheon, J, Power, IM, Shuster, J et al. (2019) Carbon Sequestration in Biogenic Magnesite and Other Magnesium Carbonate Minerals. *Environmental Science and Technology*, 53 (6). pp. 3225-3237. ISSN: 0013-936X

<https://doi.org/10.1021/acs.est.8b07055>

© 2019 American Chemical Society. This document is the unedited Author's version of a Submitted Work that was subsequently accepted for publication in *Environmental Science and Technology*, after peer review. To access the final edited and published work see <https://doi.org/10.1021/acs.est.8b07055>.

Reuse

Items deposited in White Rose Research Online are protected by copyright, with all rights reserved unless indicated otherwise. They may be downloaded and/or printed for private study, or other acts as permitted by national copyright laws. The publisher or other rights holders may allow further reproduction and re-use of the full text version. This is indicated by the licence information on the White Rose Research Online record for the item.

Takedown

If you consider content in White Rose Research Online to be in breach of UK law, please notify us by emailing eprints@whiterose.ac.uk including the URL of the record and the reason for the withdrawal request.

This document is confidential and is proprietary to the American Chemical Society and its authors. Do not copy or disclose without written permission. If you have received this item in error, notify the sender and delete all copies.

Carbon sequestration in biogenic magnesite and other magnesium carbonate minerals

Journal:	<i>Environmental Science & Technology</i>
Manuscript ID	es-2018-070555.R2
Manuscript Type:	Article
Date Submitted by the Author:	n/a
Complete List of Authors:	McCutcheon, Jenine; University of Leeds, School of Earth and Environment; Western University, Department of Earth Sciences Power, Ian; Trent University, Trent School of the Environment; The University of British Columbia, Department of Earth, Ocean and Atmospheric Sciences Shuster, Jeremiah; University of Adelaide, School of Biological Sciences; CSIRO Land and Water Harrison, Anna; Queen's University; Queen's University Dipple, Gregory; University of British Columbia, Department of Earth, Ocean and Atmospheric Sciences Southam, Gordon; The University of Queensland, School of Earth and Environmental Sciences

SCHOLARONE™
Manuscripts

Carbon sequestration in biogenic magnesite and other magnesium carbonate minerals

Jenine McCutcheon^{1,2}, Ian M. Power^{3,4}, Jeremiah Shuster^{5,6}, Anna L. Harrison^{7,8}, Gregory M.*

Dipple³, Gordon Southam⁹

¹Department of Earth Sciences, Western University, London, Ontario, N6A 5B7, Canada

²School of Earth and Environment, University of Leeds, Leeds, LS2 9JT, United Kingdom

³Department of Earth, Ocean and Atmospheric Sciences, The University of British Columbia, Vancouver, British Columbia, V6T 1Z4, Canada

⁴School of the Environment, Trent University, Peterborough, Ontario, K9L 0G2, Canada

⁵School of Biological Sciences, University of Adelaide, Adelaide, South Australia 5005, Australia

⁶CSIRO Land and Water, Glen Osmond, South Australia 5064, Australia

⁷Department of Geological Sciences and Geological Engineering, Queen's University, Kingston, Ontario, K7L 3N6, Canada

⁸School of Environmental Studies, Queen's University, Kingston, Ontario, K7L 3N6, Canada

⁹School of Earth & Environmental Sciences, The University of Queensland, St Lucia, Queensland 4072, Australia

*Corresponding contributor: j.mccutcheon@leeds.ac.uk

Keywords: carbon dioxide, cyanobacteria, magnesite, hydromagnesite, carbon sequestration, tailings, microbial carbonation, carbon pricing

1 **Abstract**

2 The stability and longevity of carbonate minerals make them an ideal sink for surplus atmospheric
3 carbon dioxide. Biogenic magnesium carbonate mineral precipitation from the magnesium-rich
4 tailings generated by many mining operations could offset net mining greenhouse gas emissions,
5 while simultaneously giving value to mine waste products. In this investigation, cyanobacteria in
6 a wetland bioreactor enabled the precipitation of magnesite (MgCO_3), hydromagnesite
7 $[\text{Mg}_5(\text{CO}_3)_4(\text{OH})_2 \cdot 4\text{H}_2\text{O}]$, and dypingite $[\text{Mg}_5(\text{CO}_3)_4(\text{OH})_2 \cdot 5\text{H}_2\text{O}]$ from a synthetic wastewater
8 comparable in chemistry to what is produced by acid leaching of ultramafic mine tailings. These
9 precipitates occurred as micrometer-scale mineral grains and microcrystalline carbonate coatings
10 that entombed filamentous cyanobacteria. This provides the first laboratory demonstration of low
11 temperature, biogenic magnesite precipitation for carbon sequestration purposes. These findings
12 demonstrate the importance of extracellular polymeric substances in microbially enabled
13 carbonate mineral nucleation. Fluid composition was monitored to determine carbon sequestration
14 rates. The results demonstrate that up to 238 t of CO_2 could be stored per hectare of wetland/year
15 if this method of carbon dioxide sequestration was implemented at an ultramafic mine tailing
16 storage facility. The abundance of tailings available for carbonation and the anticipated global
17 implementation of carbon pricing make this method of mineral carbonation worth further
18 investigation.

19

20

21

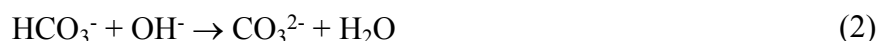
22

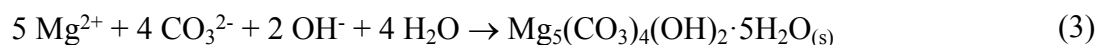
23

24 1. Introduction

25 Microbially-mediated carbonate mineral precipitation reactions, commonly referred to as
26 microbial carbonation, have been documented in numerous environments, induced by organisms
27 including cyanobacteria (1-3), sulfate reducing bacteria (4, 5), ureolytic bacteria (6, 7), and
28 oxalotrophic bacteria (8, 9). This biogeochemical process has potential to produce stable, long-
29 term sinks for atmospheric carbon dioxide (CO₂) (10-13). Stable carbonate minerals are a desirable
30 sink for atmospheric CO₂, prompting the investigation of a range of carbon sequestration strategies
31 that aim to precipitate carbonate minerals (10, 11, 14-24).

32 Passive carbonate mineral formation from ultramafic tailings produced by nickel, diamond,
33 and asbestos mining operations has been studied at active and historic mine sites (15, 25-28). The
34 high surface area of tailing minerals allows for greater weathering and carbonation reaction rates
35 than those typically observed for natural bedrock (29). The ability of cyanobacteria to mediate the
36 precipitation of hydrated magnesium carbonate minerals has been previously documented (30-32),
37 and could be stimulated by utilizing soluble magnesium derived from dissolution of ultramafic
38 tailings (13, 33). Cyanobacterial photosynthesis produces hydroxyl (OH⁻) anions that promote
39 carbonate mineral precipitation by increasing the pH value and thus the proportion of dissolved
40 carbonate (CO₃²⁻) species, as outlined in Reactions 1-3 (34). The extracellular surfaces of bacteria
41 and their encapsulating exopolymer are negatively charged due to the presence of functional
42 groups, such as carboxyls (35). These functional groups can bind divalent cations, thereby
43 generating microenvironments with high cation concentrations that favor carbonate mineral
44 precipitation reactions.





Dypingite

45

46 The present study characterizes the ability of a phototrophic microbial consortium to drive
47 Mg-carbonate mineral formation using atmospheric CO₂ in a wetland bioreactor (Figure 1). The
48 bioreactor was inoculated with microbial mats predominantly composed of filamentous
49 cyanobacteria that were collected from a natural wetland associated with a hydromagnesite-
50 magnesite playa near Atlin, British Columbia, Canada (32, 36, 37). In addition to cyanobacteria,
51 the microbial mats host abundant diatoms that remove dissolved silica from solution. The mats
52 overlie anoxic sediments known to host sulfate reducing bacteria that have been previously shown
53 to precipitate iron sulfide minerals (37). An Mg-rich synthetic mine wastewater, the chemistry of
54 which was based on a tailings leaching experiment completed by McCutcheon et al. (33), was
55 added to the bioreactor. Spatial and temporal changes in water chemistry and mineral precipitates
56 were used to calculate the rate of carbon storage, thereby demonstrating this carbon sequestration
57 strategy on a scale at least one order of magnitude greater than typical laboratory experiments.

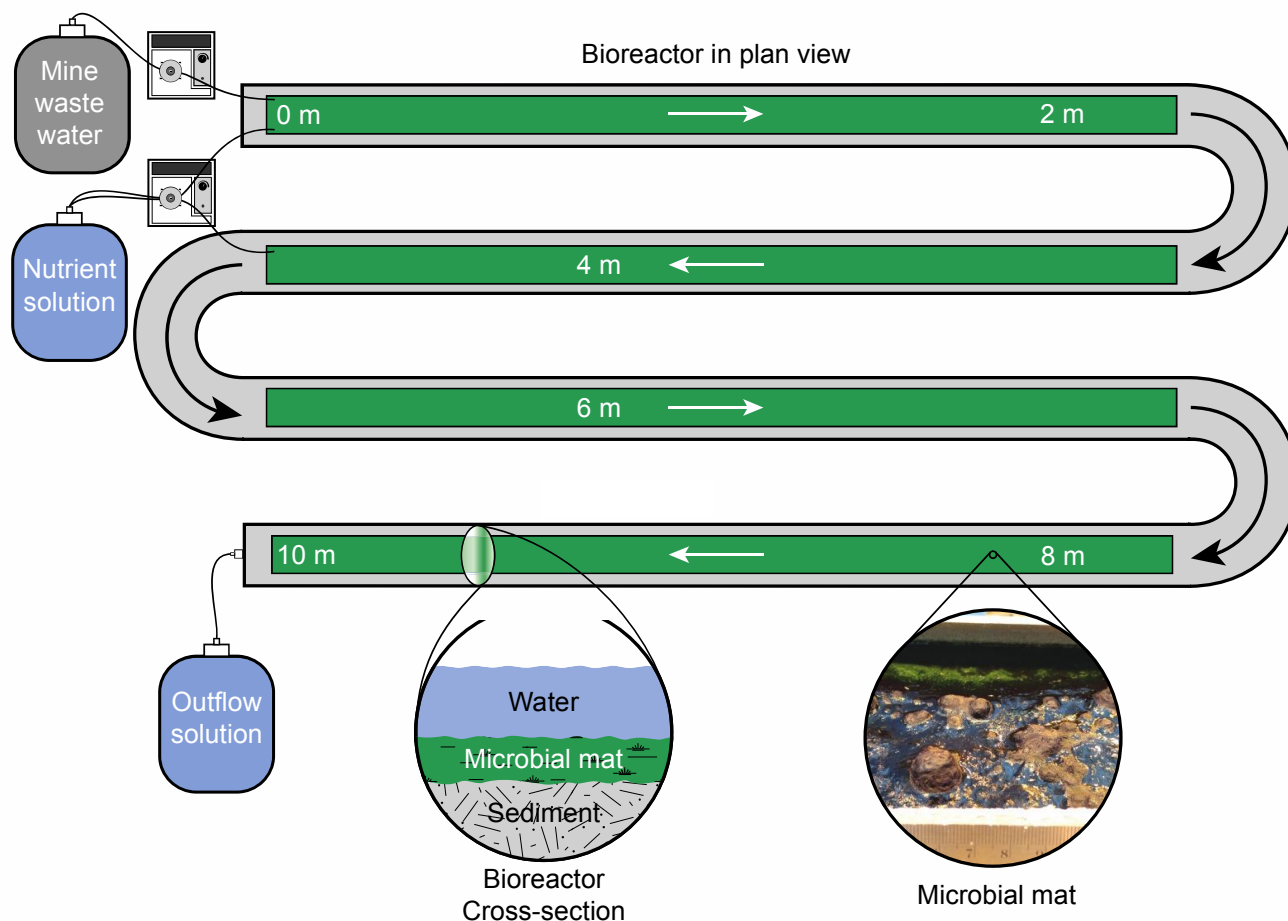
58 2. Methods

59 2.1 Bioreactor design

60 In this 67-day experiment, synthetic mine wastewater and nutrient solutions were added to
61 a 10 m long flow-through bioreactor constructed of 15 cm diameter polyvinyl chloride pipe (see
62 Supplementary Information (SI) for details). The bioreactor was initially constructed for the
63 experiment presented in McCutcheon et al. (13), in which the natural biogeochemical conditions
64 of the wetland associated with the hydromagnesite-magnesite playa near Atlin were modelled.
65 Prior to the present study, the microbial mats in the bioreactor were culled to allow for growth of

66 second generation mats containing no Mg-carbonate minerals (confirmed using electron
67 microscopy). Rather than modelling the natural wetland, the present study targeted the
68 biogeochemical conditions of an engineered mine site bioreactor wetland for the purposes of
69 maximizing carbon sequestration in Mg-carbonate minerals. A critical experimental parameter by
70 which the present study differs from its precursor is that an inorganic carbon source was not
71 provided, which is crucial as the ingress of CO₂ into mineral carbonation reactors is a known
72 limiting factor (38), and must be overcome for large-scale implementation of mineral carbonation.
73 Additionally, the synthetic mine wastewater added to the bioreactor contained 5000 ppm (205.8
74 mM) Mg²⁺. This value, which is five times greater than that used in the 2014 study, was based on
75 the results of a tailings leaching experiment (33) in order to better represent an industrial tailing
76 leachate. With dypingite as the target mineral (Reaction 3), the number of cycles of carbon fixation
77 (Reaction 1) required to make the necessary hydroxyl and carbonate anions (Reaction 3) per
78 molecule of dypingite produced was calculated as ten (13). The classic phytoplankton biomass
79 formula [(CH₂O)₁₀₆(NH₄)₁₆(H₃PO₄)] was used as a guideline to determine the phosphorous and
80 nitrogen required in the nutrient solution (39). The synthetic mine wastewater solution chemistry
81 was used to calculate the nutrient requirements of the microbes in the bioreactor using modified
82 BG-11 growth medium (SI Tables S1 and S2) (40). The solutions were added to one end of the
83 bioreactor (0 m), from which they could passively flow through the gravity-driven system and
84 drain out the other end. A second nutrient solution inflow was located at 5 m. The inflow rate of
85 both solutions was increased over time to determine the response of the bioreactor to a high influx
86 of soluble magnesium (Table 1). The bioreactor was housed in greenhouse with an average air
87 temperature of 23.5°C, as documented at all sampling time points, and subject to diurnal 12 h

88 light/dark conditions. The experiment took place in southern Canada from December to March,
 89 and thus the light was provided by a combination of natural and artificial sources.



90
 91 Figure 1. Plan view schematic of the bioreactor inoculated with microbial mats for the carbonation experiment. The
 92 synthetic mine wastewater was added at one end of the channel (0 m), while the nutrient solution was added at 0 m
 93 and 5 m. The gravity driven system allowed for the solution to flow passively through the bioreactor and out a valve
 94 in the other end. Arrows indicate the direction of flow. The four straight segments of the bioreactor were open to the
 95 air and contained the active microbial mats (green segments in the schematic), while the bends were covered. A cross-
 96 section of the bioreactor contents is shown, along with a photograph of the pellicle that formed at the air-water
 97 interface.
 98

99 After 21 days, a pellicle, a biofilm at the air-water interface, developed as sections of mat
 100 were buoyed up to the water surface by trapped photosynthetically-generated oxygen bubbles. The
 101 pellicle was removed because it was restricting the photosynthesis of the benthic microbial mats
 102 and causing a decrease in dissolved oxygen concentration in the bioreactor water. At this time, the

103 addition of the wastewater solution was ceased and the growth medium concentration was halved
 104 to moderate microbial activity (Table 1). The bioreactor outflow volume was measured to quantify
 105 evaporation, which indicated that 45% of the added water evaporated during the experiment. This
 106 water loss was taken into account for mass balance calculations for the system and when
 107 interpreting conductivity, inductively coupled plasma-atomic emission spectroscopy (ICP-AES),
 108 ion chromatography (IC), and dissolved inorganic carbon (DIC) results (SI Table S3).

109

110 Table 1. Fluid composition for the nutrient and synthetic mine wastewater solutions added to the
 111 bioreactor during the carbonation experiment. Summary of the timeline for solution addition to the
 112 bioreactor at the 0 and 5 m locations. Note, the experiment was paused between day 21 and 32 due
 113 to the formation of the pellicle.

Solution type	Fluid composition measurements			Cation and anion concentrations (mM)					
	pH	DO (mg/mL)	Conductivity (mS/cm)	Mg ²⁺	Ca ²⁺	DIC	PO ₄ ³⁻	NO ₃ ⁻	NO ₂ ⁻
100% nutrient solution	5.91	4.20	6.64	0.01	0.78	0.20	6.10	74.9	0.00
50% nutrient solution	5.91	6.11	3.65	0.00	0.34	0.20	2.28	30.7	0.00
Wastewater	8.10	7.37	18.1	196	8.16	0.21	0.00	0.00	0.00

Solution addition timeline				
Day	0 m solution addition point		5 m solution addition point	
	Solution	Flow rate (L/day)	Solution	Flow rate (L/day)
1-21	100% nutrients	1	100% nutrients	1
	Wastewater	1		
21	Experiment paused and the pellicle removed			
22-31	Standard BG-11	1	Standard BG-11	1
32	Experiment resumed			
32-38	50% nutrients	1	100% nutrients	1
	Wastewater	1		
39-45	50% nutrients	2	50% nutrients	2
	Wastewater	2		
46-52	100% nutrients	3		
	Wastewater	3		
53-59	100% nutrients	4		
	Wastewater	4		
60-67	50% nutrients	5		
	Wastewater	5		

114

115 **2.2 Mineral and microbe characterization**

116 Microbial mat samples collected at 0 m prior to the experiment, and at 0 m, 5 m, and 10 m
 117 on days 28 and 67 were analyzed using X-ray diffraction (XRD). The mats were air dried in petri
 118 dishes and powdered using a mortar and pestle. The samples were analyzed using a Bruker D8

119 Focus Bragg-Brentano diffractometer and mineral phases were determined using DIFFRAC^{plus}
120 Eva software (see SI for details). Additional microbial mat samples were collected on days 14 and
121 28 from the same locations representing upstream, midstream, and downstream mats for analysis
122 using scanning electron microscopy and energy dispersive spectroscopy (SEM-EDS; see SI for
123 details). After 67 days, microbial mats were sampled at 1 m increments for SEM-EDS. A sample
124 of microbial mat collected from the 10 m location in the bioreactor on day 67 was fixed using
125 2%_(aq) glutaraldehyde, and stained using 2%_(aq) OsO₄, 1.5%_(aq) ferricyanide, and 1%_(aq)
126 thiocarbohydrazide prior to being dehydrated using acetone, and embedded in Epon Embed 812
127 resin, described in detail in McCutcheon and Southam (41) as a protocol adapted for use on natural
128 microbial biofilms (42). Ultrathin sections of the embedded sample were characterized using
129 transmission electron microscopy (TEM) in conjunction with selected area electron diffraction
130 (SAED) and EDS (see SI for details).

131 **2.3 Fluid composition analyses**

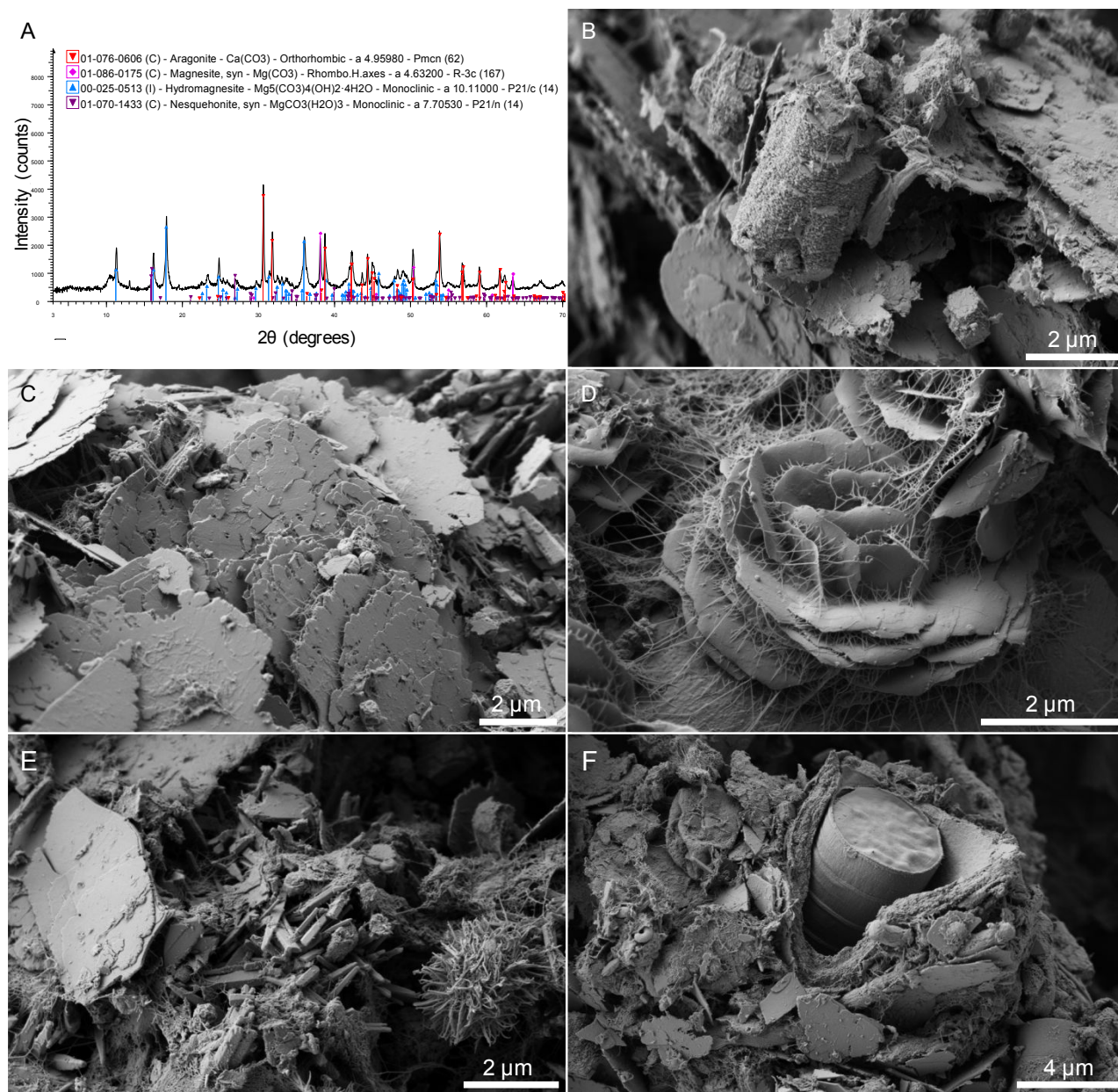
132 Fluid composition was monitored weekly at 1 m increments along the length of the
133 bioreactor. Dissolved oxygen (DO), pH, and conductivity were measured using probes (see SI for
134 details). Water samples were collected and filtered (0.1 μm pore-size) to determine DIC, and major
135 cation (ICP-AES) and anion (IC) concentrations at each location (see SI for details). Due to the
136 high concentration, magnesium was analysed using IC instead of ICP-AES. Stable carbon isotopic
137 measurements of DIC is another means of determining whether a solution is at equilibrium with
138 atmospheric CO₂ (25). Stable carbon, oxygen, and hydrogen isotope analysis was conducted on
139 water samples collected 1 week after the experiment concluded (see SI for details). Saturation
140 indices (*SI*) for possible mineral products were determined using PHREEQC (43) and the fluid

141 composition data were used to evaluate how pH, and the availability of Mg^{2+} and DIC species
142 influence carbonate mineralization (see SI for PHREEQC details).

143 **3. Results**

144 ***3.1 Carbonate mineral precipitation***

145 XRD analysis of the pre-experiment microbial mat sample identified thenardite (Na_2SO_4)
146 and aragonite ($CaCO_3$) (SI Figure S1A), neither of which were observed with SEM (SI Figure
147 S2A). Magnesite, hydromagnesite, dypingite, aragonite ($CaCO_3$), and nesquehonite
148 [$Mg(HCO_3)(OH) \cdot 2H_2O$] were identified as mineral precipitates in the bioreactor microbial mats
149 using XRD (Figure 2, SI Figure S1B,C). Subhedral rhombohedral magnesite crystals were
150 predominantly observed between 4 and 10 m in the bioreactor and were identified using TEM-
151 EDS and SAED (Figure 3A,B, SI Table S4). The magnesite often occurred at convergent points
152 between multiple hydromagnesite plates (Figure 3C-E), a relationship documented in natural
153 samples by Power et al. (36). Note the tendency of magnesite crystals to fall out of the ultrathin
154 sections, as seen in Figure 3E. For those that were retained, SAED confirms that these precipitates
155 are hexagonal, and indicates that they are polycrystalline in nature (Figure 3A,B).

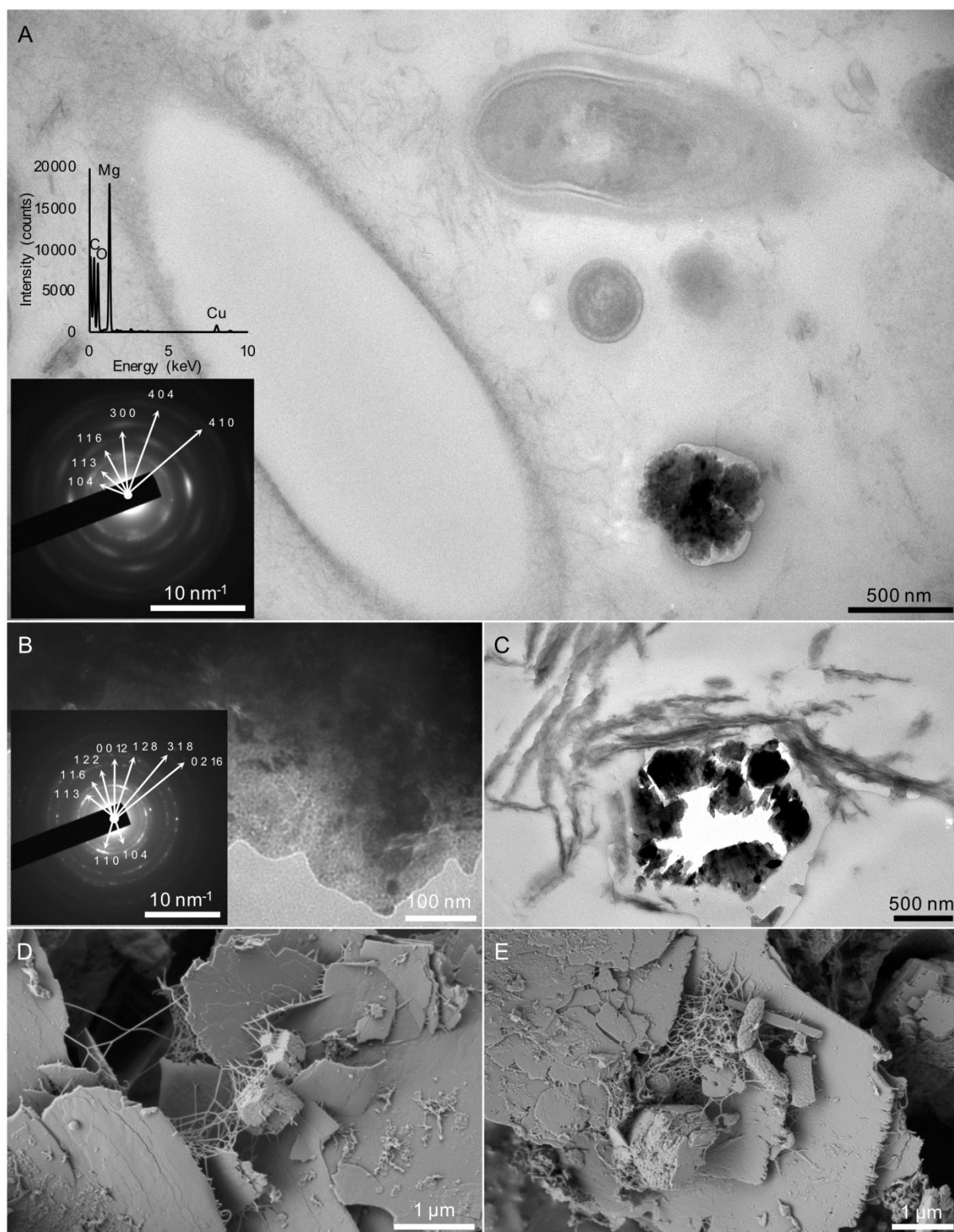


156
 157 Figure 2. X-ray diffraction and SEM results for the key mineral precipitates produced in this study. A: Pattern
 158 produced by XRD analysis of a sample of microbial mat collected at 5 m on day 67 of the carbonate precipitation
 159 experiment. Scanning electron micrographs depicting: B: rhombohedral magnesite crystals found between 4 and 10
 160 m in the bioreactor; C: platy hydromagnesite or dypingite crystals formed throughout the bioreactor; D: a rosette of
 161 hydromagnesite or dypingite covered in EPS (day 67, 1 m); E: platy hydromagnesite or dypingite crystal (left),
 162 disarticulated aragonite crystals (centre), and mineral coated coccoid bacterium (right); and F: cyanobacterium
 163 filament encased in Mg-carbonate encrusted EPS (day 14, 10 m).
 164

165 Hydromagnesite or dypingite crystals were the most abundant precipitates and occurred as
 166 plates and rosettes, often associated with large amounts of extracellular polymeric substances
 167 (EPS; Figure 2C,D). The EPS exhibits the collapsed, mesh-like morphology commonly observed

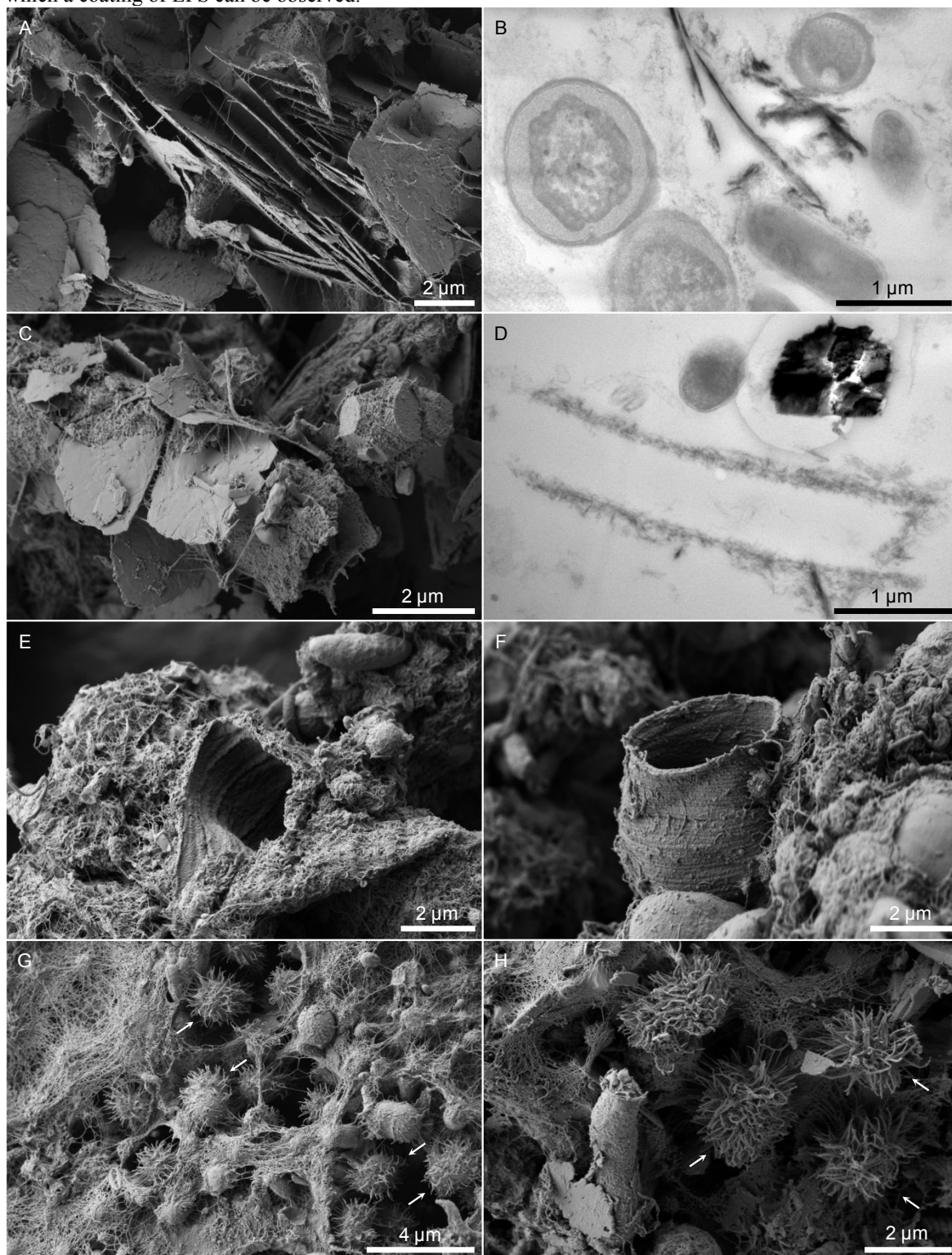
168 when biofilms are prepared for SEM via solvent dehydration and critical point drying (41). The
169 platy hydromagnesite or dypingite precipitates visible using SEM (Figure 4A) can also be observed
170 using TEM, oriented tangential to the filamentous cells such that only the edge of the platy crystals
171 can be observed (Figure 4B). The platy precipitates can be observed nucleating on EPS
172 surrounding filamentous cyanobacteria (Figure 4B,C), as demonstrated by McCutcheon and
173 Southam (41). In addition to crystalline precipitates, cells and surrounding EPS often appear coated
174 in microcrystalline precipitates (Mg-C-O based on EDS), resulting in cells becoming entombed
175 (Figure 2F), likely interfering with microbial metabolism. Many empty Mg-carbonate casts
176 exhibiting the morphology of cyanobacterium filaments were observed using TEM (Figure 4D)
177 and SEM (Figure 4E,F), appearing to encase a framework of EPS. Poorly crystallized ~100 nm-
178 scale pseudo-acicular precipitates composed of Ca-Mg-C-O-P formed directly on coccoid
179 microbial cells (Figure 2E, 4G,H), much like the extracellular precipitate morphology observed by
180 Shuster et al. (44).

181 Aragonite was observed as prismatic crystals (SI Figure S2B,C), similar to those
182 documented by Power et al. (37) from sediments in the Atlin wetland (See SI for aragonite and
183 nesquehonite results). Struvite ($\text{NH}_4\text{MgPO}_4 \cdot 6\text{H}_2\text{O}$) was identified in the samples collected from
184 the bioreactor, with this mineral phase being most abundant at 0 m and 5 m (SI Figure S2E,F).



185
186 Figure 3. Transmission electron micrographs showing A: the microbial biofilm in ultrathin section, including a
187 magnesite grain (corresponding SAED pattern and spectrum on left) adjacent to the EPS outline of a cell; B:
188 a magnesite grain in ultrathin section with corresponding SAED (inlay); and C: a magnesite grain (centre)
189 at the junction between platy hydromagnesite crystals. Note the tendency of magnesite to fall out of the ultrathin section (C). D and

190 E: Secondary electron micrographs depicting the same magnesite-hydromagnesite relationship visible in (C), over
 191 which a coating of EPS can be observed.



192 Figure 4. A: Secondary electron micrograph showing the platy hydromagnesite crystals. B: Transmission electron
 193 micrograph showing platy hydromagnesite crystals as they nucleate on EPS adjacent to filamentous cyanobacteria
 194 (visible here in cross-section). EPS-nucleated hydromagnesite and mineral encrusted EPS outlining cyanobacterium
 195 filaments visible using C: SEM and D: TEM. Note the magnesite crystal visible in the top right corner of both C and
 196

197 D, E and F: Casts of filamentous bacteria composed of magnesium carbonate. Scanning electron micrographs of G:
198 the large amount of EPS generated in the bioreactor along with the microcrystalline pseudo-acicular mineral
199 precipitate (H) found coating coccoid cells within the microbial mat (coated cells indicated by arrows in G and H).
200

201 **3.2 Fluid composition**

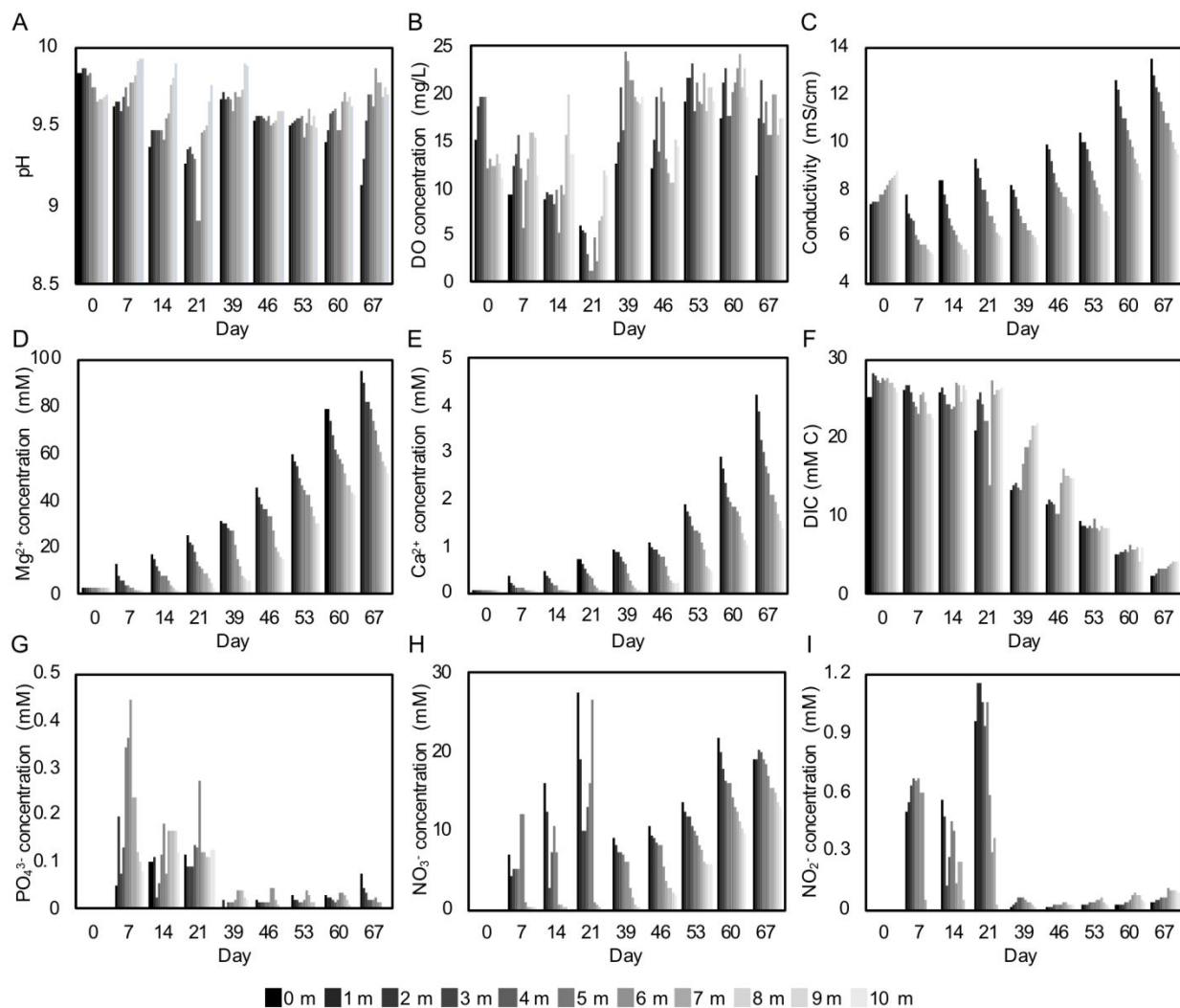
202 The pH and DO concentrations both decreased during the first 21 days of the experiment,
203 coincident with the formation of the pellicle, from respective system averages of 9.8 and 15.2 mg/L
204 on day 0, to 9.4 and 5.9 mg/L on day 21 (Figure 5A,B; SI Table S5). The conductivity, and Mg^{2+}
205 and Ca^{2+} concentrations increased over time with the increase in flow rate from day 39 to 67, while
206 spatially, these three parameters decreased down the length of the bioreactor (Figure 5C-E). With
207 a wastewater inflow rate of 1 - 3 L/day, the bioreactor precipitated carbonate minerals at a rate that
208 reduced the conductivity and magnesium concentration to equal or less than the Time = 0 values
209 (Figure 5C-E). Conductivity (Figure 5C) and magnesium concentration (Figure 5D) values
210 increased with inflow rates of 4 and 5 L/day despite magnesium continuously being removed from
211 the water, suggesting the influx exceeded the rate of removal via precipitation. The average
212 magnesium concentration of the entire bioreactor increased from 2.6 mM to 68.8 mM over time,
213 owing to the increased inflow rate (Figure 5D, SI Table S5).

214 The DIC was relatively constant during the first 21 days, after which it decreased as the
215 wastewater inflow rate was increased (Figure 5F; SI Table S5). DIC concentrations increased with
216 distance from the source of nutrient and synthetic mine wastewater input at 0 m and 5 m. Higher
217 nutrient availability at these locations may have caused localized increases in heterotrophy;
218 however, it appears that autotrophy dominated the microbial activity beyond 5 m, resulting in a
219 pH value increase due to photosynthesis driven CO_2 consumption and OH^- generation. The DIC
220 concentration on day 67 was 64% of what was measured on day 60, indicating rapid removal of

221 DIC from solution via carbonate precipitation (SI Table S5). Note, approximately 11% of this
222 decrease is due to the increase in flow rate.

223 The phosphate concentration showed no clear trend during the first 21 days of the
224 experiment, apart from a clear increase in concentration at the 5 m sampling location,
225 corresponding to the second nutrient addition point (Figure 5G; SI Table S5). From day 39 to 67,
226 the phosphate concentration approached 0, and never increased above 0.1 mM. The nitrate
227 concentration was irregular during the first 21 days, after which nitrate accumulated over time to
228 a system average concentration of 17.3 mM on day 67 (Figure 5H). The nitrate concentration
229 decreased down the length of the bioreactor. No nitrite was measured in the nutrient solution or
230 mine wastewater (Table 1). The nitrite concentration was irregular in the bioreactor during the first
231 21 days, fluctuating between 0.04 and 1.15 mM (Figure 5I). From day 39 to 67, the nitrite
232 concentration decreased markedly to less than 0.1 mM (Figure 5I; SI Table S5).

233



234
 235 Figure 5. Change in the fluid composition parameters down the length of the bioreactor over the
 236 duration of the experiment. A) pH, B) dissolved oxygen, C) conductivity, D) Mg^{2+} , E) Ca^{2+} , F)
 237 DIC, G) phosphate, H) nitrate, and I) nitrite. Note, no phosphate, nitrate, or nitrite data is available
 238 for day 0.
 239

240 On day 67, the $\delta^{2}\text{H}$ and $\delta^{18}\text{O}$ values of the water increased with distance down the
 241 bioreactor length (Table 2). The equilibrium fractionation between $\text{CO}_{2(\text{g})}$ and HCO_3^- , the
 242 dominant DIC species at the experimental pH, is +7.9% at 25°C (45), and the $\delta^{13}\text{C}$ value of
 243 atmospheric CO_2 is approximately -8.3% (46). The stable carbon isotope analysis indicated that
 244 the $\delta^{13}\text{C}_{\text{DIC}}$ was -6.76% at 0 m and decreased down the length of the bioreactor to -9.04% at 10

245 m (Table 2), while the DIC concentration increased from 2.42 to 4.16 mM over the same distance
 246 (SI Table S5).

247
 248 Table 2. Stable isotope data for water samples collected following the carbonate precipitation
 249 experiment.

Sample location	$\delta^{13}\text{C}$ (‰)	$\delta^2\text{H}$ (‰)	$\delta^{18}\text{O}$ (‰)
0 m	-6.76	-27.3	-0.32
1 m	-7.17	-31.12	0.08
2 m	-7.99	-28.93	0.12
3 m	-9.15	-23.38	0.27
4 m	-8.97	-27.3	0.47
5 m	-9.35	-23.3	0.24
6 m	-8.99	-26.57	1.25
7 m	-8.59	-27.28	1.43
8 m	-8.77	-23.7	2.09
9 m	-8.92	-20.62	2.64
10 m	-9.04	-14.9	2.43

250
 251 Carbonate mineral Saturation Indices (*SI*) were calculated using the fluid composition data
 252 and PHREEQC (SI Tables S6-24). The synthetic mine wastewater had *SI*s for hydromagnesite and
 253 magnesite of -10.07 and -0.65, respectively. On day 0, the sampling locations in the bioreactor had
 254 hydromagnesite and magnesite *SI*s ranging between -0.36 and 0.51, and 1.39 and 1.45,
 255 respectively. The average hydromagnesite *SI* for the bioreactor increased from 0.05 (day 0) to 3.64
 256 (day 39) followed by a decrease over the remainder of the experiment. The system average *SI* for
 257 magnesite increased over time from 1.43 on day 0 to 2.09 on day 39, followed by a decrease to
 258 1.62 by day 67 (SI Table S23). The average magnesite *SI* by sampling location changed little over
 259 time, remaining between 1.72 and 1.86. On the final day of the experiment (day 67), the magnesite
 260 *SI* increased down the length of the bioreactor from 1.2 (0 m) to 1.81 (10 m). The bioreactor did
 261 not reach equilibrium with atmospheric $p\text{CO}_{2(\text{g})}$ at any point during the experiment (SI Table S19).
 262 The calculated $p\text{CO}_2$ in equilibrium with the measured DIC values was in the range of 1.0 to 158
 263 ppm (SI Table S19).

264

265 **4. Discussion**266 **4.1 Microbial magnesium carbonate mineral precipitation**

267 The trends observed between Mg-carbonate type and location in the bioreactor can be
268 explained using Ca-carbonate precipitation kinetics (47-50), as carbonate crystal size and
269 abundance is dependent on the balance between crystal nucleation rate and crystal growth rate.
270 Higher degrees of supersaturation promote mineral nucleation, resulting in a greater abundance of
271 individual crystals (48, 50), a relationship observed in the upper 5 m of the bioreactor as rapid
272 nucleation of the microcrystalline coatings on microbial cells. In contrast, crystal growth is favored
273 over crystal nucleation in solutions with a low degree of supersaturation and results in fewer, larger
274 crystals. This relationship is evident in the downstream 5 m of the bioreactor, where micrometer-
275 scale hydromagnesite and magnesite grains were the prevailing precipitates.

276 Microbial mats aid carbonate mineral nucleation, in part, by assisting the dehydration of
277 divalent cations. This is a particularly critical precursor in the case of Mg-carbonates, which are
278 more difficult to precipitate than their calcium counterparts. Mg^{2+} ions in solution are enclosed in
279 a stable hydration shell composed of two layers of water molecules (51, 52). The inner layer
280 consists of an octahedrally coordinated shell of six water molecules, around which a second shell
281 of twelve water molecules is bound by hydrogen-bonds (52-54). The hydration energy of
282 magnesium (1926 kJ/mol) compared to calcium (1579 kJ/mol) results in water molecule exchange
283 in calcium's hydration shell occurring $\sim 1000\times$ faster than around magnesium (55, 56), resulting in
284 much lower precipitation rates of anhydrous Mg-carbonates compared to Ca-carbonates, and thus
285 the tendency to form hydrated Mg-carbonates at low temperature. The biogenic process by which
286 the magnesite identified using TEM-SAED-EDS formed explains why the lattice spacings for

287 these precipitates do not precisely match reference values (57) (Figure 3, SI Table S4). Biogenic
288 carbonate minerals tend to exhibit a higher degree of crystal lattice disorder than their abiotically
289 synthesized counterparts (58, 59), a characteristic that is detectable using SAED (60).

290 Abiotic precipitation of magnesite at temperatures below 80°C is typically inhibited by the
291 energy required for the spiral step crystal growth pattern by which magnesite forms (61).
292 However, Power et al. (51) demonstrated that the hydration shell surrounding Mg^{2+} ions can be
293 disrupted by binding to carboxyl-coated polystyrene microspheres, thereby inducing low
294 temperature magnesite precipitation. The results of the present study demonstrate that the
295 negatively charged cell exteriors and EPS in cyanobacterial mats are capable of facilitating Mg^{2+}
296 dehydration through a similar mechanism (32). As much as 90% of the total organic carbon in
297 biofilms is found in the EPS, which comprises a matrix of water, polysaccharides, lipids, proteins,
298 and nucleic acids (62). Extracellular polysaccharides provide a large proportion of the stability of
299 biofilms (63), which is influenced by the prevalence of cation binding. Cross-linking of
300 polysaccharides in the EPS with cations can increase biofilm stability, while simultaneously
301 generating localized microenvironments of high cation concentrations (64). The EPS becomes a
302 cation reservoir to which low molecular weight (LMW) organic compounds can attach.
303 Heterotrophic metabolic processes oxidize these LMW compounds to product bicarbonate, which
304 can subsequently react with the cations to form carbonate minerals (64). Mineral precipitates may
305 remain attached to the EPS, as in the case of the cellular carbonate coatings (Figure 4C), or be
306 released like many of the hydromagnesite plates observed using SEM (Figure 4A). The apparent
307 tendency for hydromagnesite to nucleate on, and subsequently be shed from, EPS was
308 demonstrated by McCutcheon and Southam (41), and highlights that microbial mats must be
309 actively producing and metabolizing EPS to provide carbonate mineral nucleation sites.

310 Carbonate precipitation can lead to mat lithification, a process demonstrated in the rock
311 record and many contemporary environments (4, 65-67). For the reasons outlined above, calcium,
312 rather than magnesium, carbonate minerals are the predominant deposits found in natural settings
313 and throughout the rock record. The formation of magnesite, versus less stable, hydrated Mg-
314 carbonate mineral phases is likely dependant on the optimization of a number of factors, namely:
315 the efficiency of the biogeochemical process of cation dehydration described above, development
316 of EPS-hosted microenvironments of high Mg^{2+} concentration, and alkalinity generation via
317 microbial metabolism. Hydrated Mg-carbonate minerals, such as hydromagnesite, typically
318 dominate known Mg-carbonate deposits because the magnesium ions need not be completely
319 dehydrated (61, 68), thus making the successful demonstration of low temperature, microbially-
320 aided magnesite precipitation in the present study noteworthy.

321 ***4.2 Microbial activity and fluid composition***

322 Some of the CO_2 used in carbonate precipitation may have been generated by heterotrophic
323 oxidation of photosynthetically-derived organic compounds, and contributed to DIC by producing
324 dissolved CO_2 or HCO_3^- (12, 69). Organic matter in microbial mat systems is largely derived from
325 atmospheric carbon fixed by phototrophs, which can be oxidized by heterotrophs, providing an
326 indirect pathway for transferring atmospheric CO_2 into water (12). Heterotrophic activity,
327 therefore, may have been partially responsible for the patterns observed in the DIC, a possibility
328 supported by the depletion in $^{13}C_{DIC}$ (70). Phototrophic metabolism preferentially removes $^{12}C_{DIC}$
329 thereby enriching the remaining DIC pool in ^{13}C while decreasing DIC concentrations (71).
330 Carbonate precipitation may decrease both DIC concentration and $\delta^{13}C_{DIC}$ values (25). However,
331 for the majority of the bioreactor length, $\delta^{13}C_{DIC}$ values and DIC generally co-vary, likely due to
332 dissolution of atmospheric CO_2 , as this will increase both DIC and $\delta^{13}C$ values. Progressive

333 increases in $\delta^2\text{H}$ and $\delta^{18}\text{O}$ from -27.3‰ and -0.3‰ to -14.9‰ and 2.4‰, respectively, can be
334 attributed to evaporation along the length of the bioreactor (Table 2) (72).

335 Saturation indices cannot be used as strict indicators of Mg-carbonate precipitation, given
336 kinetic limitations to precipitation; however, the following interpretations regarding the
337 relationship between fluid composition, *SI*, and mineral precipitation can be made (13). The
338 changes in magnesium concentration indicated that the greatest carbonation rate was achieved
339 from day 60 - 67 and carbonate precipitation was pervasive throughout the bioreactor. The low
340 hydromagnesite *SI* values calculated for day 67 are consistent with rapid mineral precipitation and
341 may be responsible for the observed cyanobacteria entombment. The pH and DO measurements
342 from days 60 and 67 suggest that this mineralization caused a decline in photosynthesis, with the
343 system average pH value decreasing from 9.59 to 6.21, and system average DO from 21.0 mg/L
344 to 17.4 mg/L (SI Table S5). Addition of 5000 ppm magnesium at a rate of 5 L/day was likely
345 approaching the limit of the bioreactor's ability to consume magnesium; therefore, reducing the
346 flow rate or the magnesium concentration would be necessary for long-term maintenance of the
347 biogeochemical conditions required for carbonation.

348 The pellicle likely limited gas exchange between the atmosphere and bioreactor water, as
349 well as photosynthesis in the submerged microbial mats. Reduced photosynthesis plus
350 heterotrophic consumption of oxygen resulted in a suboxic environment that potentially stimulated
351 sulfate reducing-bacteria (SRB) activity, organisms previously found in the anoxic sediments used
352 to line the bottom of the bioreactor (37). These organisms use sulfate (SO_4^{2-}) as a terminal electron
353 acceptor to oxidize organic compounds, producing hydrogen sulfide (H_2S) (73, 74), which can
354 consume oxygen, support anoxygenic photosynthesis, and/or be toxic to cyanobacteria (75-77).
355 The metabolic activity of SRBs would have increased as DO decreased, especially at night (75).

356 While SRBs can enable carbonate precipitation by driving the water chemistry conditions towards
357 carbonate supersaturation and generating EPS (4, 5), the toxicity of H₂S towards cyanobacteria
358 was likely detrimental to the overall bioreactor function (78). Thus, the pellicle formation
359 demonstrates the need to regulate nutrient input, microbial growth, and carbonate precipitation,
360 such that biofilm formation does not outpace the bioreactor's capabilities.

361 The elevated concentration of nitrite during the initial 21 days of the experiment (Figure
362 5I) is consistent with nitrate consumption by denitrifying bacteria in anaerobic biofilms (79),
363 which would be enabled by the low DO conditions caused by the pellicle. Nitrite is part of active
364 nitrogen fixation-nitrification-denitrification reaction pathway common in cyanobacteria-
365 dominated microbial mats. The nitrite depletion that occurred following the removal of the pellicle
366 and corresponding reoxygenation of the water suggests that anaerobic denitrification was the
367 source of the nitrite (80). The disappearance of nitrite after day 21, corresponding to the loss of
368 the pellicle and re-oxygenation of the bioreactor suggests that denitrification was the source of the
369 nitrite.

370 ***4.3 Quantifying mineral precipitation rate and application to carbon sequestration***

371 This study demonstrated that atmospheric CO₂ can be sequestered via microbial
372 carbonation in an engineered system, which is important because dissolution of atmospheric CO₂
373 into water is typically the rate-limiting step in mineral carbonation experiments and in mine
374 tailings (14, 25). The water chemistry data, flow rate, and microbial mat surface area were used to
375 calculate mineral precipitation and carbon storage rates. Carbon storage in biomass is considered
376 in addition to storage in mineral phases; as its presence was minimal, aragonite was excluded from
377 the storage calculation. See SI for details regarding how struvite precipitation was accounted for
378 in the biomass calculation.

379 The first week (day 0-7; inflow: 1 L/day) of the experiment exhibited the highest proportion
380 of magnesium removed (98%); however, the greatest mass of carbonate precipitated occurred
381 during the final week of the experiment (day 60-67; inflow: 5 L/day) with 73% of the added
382 magnesium being used for carbonate precipitation. During the final week, 5.05 mol or ~123 g of
383 Mg was used to produce carbonate minerals. A carbon sequestration rate can be calculated for each
384 of hydromagnesite and magnesite, providing a range for mineral carbonation. It was calculated
385 that 472 g of hydromagnesite or 426 g of magnesite could have formed in the bioreactor during
386 the final week. Extrapolating this process to the scale of a microbial carbonation wetland at a mine
387 tailings storage facility, these values translate to combined biomass and mineralogical carbon
388 storage rates of 222 and 238 t of CO₂/ha of wetland/year for hydromagnesite and magnesite,
389 respectively. The hydration of hydromagnesite results in a slightly greater precipitate mass when
390 compared to magnesite, but makes it slightly less efficient in terms of carbon stored per magnesium
391 atom.

392 The undersaturation of the bioreactor water with respect to atmospheric CO₂ suggests that
393 sequestration rates could be increased by providing additional carbon. Harrison et al. (14)
394 demonstrated that supplying gas containing 10% CO₂, similar to power plant flue gas, causes a
395 240-fold increase in the rate of Mg-carbonate mineral precipitation in brucite [Mg(OH)₂]-bearing
396 slurries. Limited availability of water in dry tailings can also inhibit hydrated magnesium
397 carbonate mineral precipitation (81). An in situ microbial mineral carbonation experiment by
398 McCutcheon et al. (82) demonstrated the challenge of water limitation, in which a microbial
399 inoculum, cultured from biofilms naturally occurring at the mine site, was added to chrysotile mine
400 tailings for the purpose of producing a Mg-carbonate crust. Those results indicated that
401 constructing microbial carbonation wetlands, similar to the one implemented in the present study,

402 is likely the best strategy for integrating microbial carbonation technology for industrial carbon
403 sequestration at tailing storage facilities (82). A potential deployment strategy would include the
404 production Mg-rich fluids via large-scale leaching of mafic or ultramafic mine tailings, which
405 would act as a feedstock for carbonation wetlands that could be constructed in the open pits
406 remaining from mining activity (82). Carbonate mineral precipitation in the wetlands could utilize
407 atmospheric CO₂, while simultaneously sequestering first row transition metals that may be
408 released from the tailings during acid leaching, thus reducing the risk of toxic metal contamination
409 of the surrounding environment (83, 84). Similar to the wetland near Atlin, which hosts sulfate
410 reducing bacteria in the underlying anoxic sediments, any sulfate accumulating in the system
411 could be consumed through iron sulphide mineral generation by SRBs (37).

412 Microbial mat lithification would occur as a more laterally extensive variation of the
413 cementation observed in naturally occurring stromatolites, exhibiting progressive growth and
414 cementation over time. The mats would grow upwards as lithification progresses, maintaining an
415 active layer of microbial mat into which the ion-rich leach solution can infiltrate, thereby receiving
416 the reactants required for carbonate precipitation. Through this process, the pit would gradually
417 become infilled with the resulting precipitates, forming a carbonate deposit. The stability of the
418 deposit should be monitored in order to ensure safe mine site reclamation.

419 As a measure of scale for the deployment of this carbon sequestration strategy, applying
420 this technology to the Mount Keith Nickel Mine (Western Australia) would require a 1900 ha
421 bioreactor, a size comparable to the existing tailings facility. Such a wetland could sequester
422 000 to 450 000 t of CO₂/year, which is ~10% of the estimated 4 Mt CO₂/year sequestration capacity
423 of the Mount Keith tailings facility (85). The remaining capacity could be satisfied using other
424 acceleration strategies, such as flue gas injection (14). In 2004, the Mount Keith Mine emitted

425 ~382 000 t of CO₂ equivalent, demonstrating that the proposed carbon storage strategy is capable
426 of sequestering mine-scale quantities of CO₂ (12). With the correct balance of nutrients, e.g., the
427 limiting phosphate concentrations encountered in this study (Fig. 5), microbial growth and mine
428 wastewater input, the carbonate precipitation rate could be increased. If successful, this technology
429 could fulfil a portion of the ~175 Mt CO₂/year total carbon sequestration capacity estimated for
430 the ~419 Mt of mafic and ultramafic tailings that are generated worldwide each year (86, 87).

431 The lack of a global carbon price is a fundamental limiting condition for the development
432 of mineral carbonation strategies beyond laboratory demonstrations for large-scale industrial
433 implementation (86), however, estimates by the High-Level Commission on Global Carbon Prices
434 indicate that meeting the temperature target of the Paris Agreement will necessitate carbon prices
435 of \$50-100 USD/t CO₂ by 2030 (88). At a conservative price of \$50 USD/t, economic valuation
436 of microbial carbonation of nickel mine tailings, considering past production and reserve ore at
437 major ultramafic nickel mine sites worldwide (excluding other ultramafic mine tailings), puts the
438 prospective worth of this microbial carbon storage technology at \$20.5 billion USD (89, 90). Such
439 a valuation is encouraging, as it will be necessary for many countries to increase their carbon price
440 to achieve their emission reduction targets (88). For instance, the fuel levy rates currently
441 implemented in Canada as part of the federal carbon pricing backstop equate to \$10 CAD/t
442 CO_{2(equivalent)} for 2018, and are due to increase by \$10 CAD/year until a price of \$50 CAD/t
443 CO_{2(equivalent)} is reached in 2022 (91). Meeting the International Energy Agency (IEA) '2°C
444 Scenario' may result in global marginal abatement costs reaching \$130-160 USD/t CO₂ by 2050
445 (88, 92), providing incentive for pursuing cost-effective implementation of various mineral
446 carbonation technologies. Additional value could be gained during the implementation of

447 microbial carbonation wetland bioreactors by integrating the biomass component of this carbon
448 sequestration method with biofuel production technologies (93, 94).

449

450 **5. Acknowledgements**

451 We acknowledge funding support provided by: Natural Sciences and Engineering Research
452 Council of Canada (NSERC Discovery) (G.S.), Carbon Management Canada (G.M.D. and G.S.),
453 Ontario Graduate Scholarship (J.M.), and NSERC Canada Graduate Scholarship (J.M.). For their
454 technical assistance, we thank Todd Simpson and Tim Goldhawk of the Western Nanofabrication
455 Facility (SEM); Kathryn Green, Richard Webb, Robyn Webb, and Graeme Auchterlonie of the
456 Centre for Microscopy and Microanalysis, The University of Queensland (TEM); and Charles Wu
457 (ICP-AES) and Monique Durr (IC) of the Biotron Institute for Experimental Climate Change
458 Research Analytical Chemistry laboratory. DIC analyses were conducted at The University of
459 British Columbia. Stable isotope analyses were conducted at the G.G. Hatch Stable Isotope
460 Laboratory at The University of Ottawa.

461

462 **Supporting Information**

463 The supplementary information file contains details about the experimental design and the
464 composition of the nutrient and synthetic mine wastewater solutions added to the bioreactor. It
465 reports the errors for the fluid composition measurements and analyses. It also contains additional
466 methods and results for the fluid composition, X-ray diffraction, and electron microscopy analyses,
467 and tables of PHREEQC input data and saturation index outputs.

468

469 **References**

- 470 1. Boquet, E.; Boronat, A.; Ramosco, A. Production of calcite (calcium-carbonate) crystals
471 by soil bacteria is a general phenomenon. *Nature* **1973**, *246* (5434), 527-529; 10.1038/246527a0.
- 472 2. Merz, M. The biology of carbonate precipitation by cyanobacteria. *Facies* **1992**, *26*, 81-
473 102.
- 474 3. Riding, R. Microbial carbonates: the geological record of calcified bacterial-algal mats and
475 biofilms. *Sedimentology* **2000**, *47*, 179-214.
- 476 4. Braissant, O.; Decho, A. W.; Dupraz, C.; Glunk, C.; Przekop, K. M.; Visscher, P. T.
477 Exopolymeric substances of sulfate-reducing bacteria: Interactions with calcium at alkaline pH
478 and implication for formation of carbonate minerals. *Geobiology* **2007**, *5*, 401-411;
479 10.1111/j.1472-4669.2007.00117.x.
- 480 5. Gallagher, K.; Kading, T. J.; Braissant, O.; Dupraz, C.; Visscher, P. T. Inside the alkalinity
481 engine: The role of electron donors in the organomineralization potential of sulfate-reducing
482 bacteria. *Geobiology* **2012**, *10*, 518-530; 10.1111/j.1472-4669.2012.00342.x.
- 483 6. Ferris, F. G.; Phoenix, V.; Fujita, Y.; Smith, R. W. Kinetics of calcite precipitation induced
484 by ureolytic bacteria at 10 to 20°C in artificial groundwater. *Geochim. Cosmochim. Acta* **2004**, *68*
485 (8), 1701-1710; [https://doi.org/10.1016/S0016-7037\(03\)00503-9](https://doi.org/10.1016/S0016-7037(03)00503-9).
- 486 7. Mitchell, A. C.; Ferris, F. G. The influence of *Bacillus pasteurii* on the nucleation and
487 growth of calcium carbonate. *Geomicrobiol. J.* **2006**, *23* (3-4), 213-226;
488 10.1080/01490450600724233.
- 489 8. Braissant, O.; Cailleau, G.; Aragno, M.; Verrecchia, E. P. Biologically induced
490 mineralization in the tree *Milicia excelsa* (Moraceae): its causes and consequences to the
491 environment. *Geobiology* **2004**, *2* (1), 59-66; 10.1111/j.1472-4677.2004.00019.x.
- 492 9. Cailleau, G.; Braissant, O.; Dupraz, C.; Aragno, M.; Verrecchia, E. P. Biologically induced
493 accumulations of CaCO₃ in orthox soils of Biga, Ivory Coast. *Catena* **2005**, *59* (1), 1-17;
494 <http://dx.doi.org/10.1016/j.catena.2004.06.002>.
- 495 10. Power, I. M.; Dipple, G. M.; and Southam, G. Bioleaching of ultramafic tailings by
496 *Acidithiobacillus* spp. for CO₂ sequestration. *Environ. Sci. Technol.* **2010**, *44*, 456-462;
497 10.1021/es900986n.
- 498 11. Power, I. M.; Wilson, S. A.; Dipple, G. M.; Southam, G. Modern carbonate microbialites
499 from an asbestos open pit pond, Yukon, Canada. *Geobiology* **2011**, *9*, 180-195; 10.1111/j.1472-
500 4669.2010.00265.x.
- 501 12. Power, I. M.; Wilson, S. A.; Small, D. P.; Dipple, G. M.; Wan, W.; Southam, G.
502 Microbially mediated mineral carbonation: Roles of phototrophy and heterotrophy. *Environ. Sci.*
503 *Technol.* **2011**, *45*, 9061-9068; dx.doi.org/10.1021/es201648g.
- 504 13. McCutcheon, J.; Power, I. M.; Harrison, A. L.; Dipple, G. M.; Southam, G. A greenhouse-
505 scale photosynthetic microbial bioreactor for carbon sequestration in magnesium carbonate
506 minerals. *Environ. Sci. Technol.* **2014**, *48* (16), 9142-9151; dx.doi.org/10.1021/es500344s.
- 507 14. Harrison, A. L.; Power, I. M.; Dipple, G. M. Accelerated carbonation of brucite in mine
508 tailings for carbon sequestration. *Environ. Sci. Technol.* **2013**, *47* (1), 126-134;
509 dx.doi.org/10.1021/es3012854.
- 510 15. Wilson, S. A.; Dipple, G. M.; Power, I. M.; Thom, J. M.; Anderson, R. G.; Raudsepp, M.;
511 Gabite, J. E.; Southam, G. Carbon dioxide fixation within mine wastes of ultramafic-hosted ore
512 deposits: Examples from the Clinton Creek and Cassiar chrysotile deposits, Canada. *Econ. Geol.*
513 **2009**, *104*, 95-112.

- 514 16. Washbourne, C. L.; Renforth, P.; Manning, D. A. C. Investigating carbonate formation in
515 urban soils as a method for capture and storage of atmospheric carbon. *Sci. Total Environ.* **2012**,
516 *431*, 166-175; 10.1016/j.scitotenv.2012.05.037.
- 517 17. Teir, S.; Eloneva, S.; Zevenhoven, R. Production of precipitated calcium carbonate from
518 calcium silicates and carbon dioxide. *Energy Conversion and Management* **2005**, *46* (18), 2954-
519 2979; <https://doi.org/10.1016/j.enconman.2005.02.009>.
- 520 18. Zhao, H.; Park, Y.; Lee, D. H.; Park, A. H. Tuning the dissolution kinetics of wollastonite
521 via chelating agents for CO₂ sequestration with integrated synthesis of precipitated calcium
522 carbonates. *Phys. Chem. Chem. Phys.* **2013**, *15* (36), 15185-92; 10.1039/c3cp52459k.
- 523 19. Huijgen, W. J. J.; Witkamp, G.-J.; Comans, R. N. J. Mechanisms of aqueous wollastonite
524 carbonation as a possible CO₂ sequestration process. *Chem. Eng. Sci.* **2006**, *61* (13), 4242-4251;
525 <https://doi.org/10.1016/j.ces.2006.01.048>.
- 526 20. Gerdemann, S. J.; O'Connor, W. K.; Dahlin, D. C.; Penner, L. R.; Rush, H. Ex situ aqueous
527 mineral carbonation. *Environ. Sci. Technol.* **2007**, *41*, 2587-2593.
- 528 21. Park, A.-H. A.; Fan, L.-S. CO₂ mineral sequestration: Physically activated dissolution of
529 serpentine and pH swing process. *Chem. Eng. Sci.* **2004**, *59*, 5241-5247;
530 10.1016/j.ces.2004.09.008.
- 531 22. Park, A. H. A.; Jadhav, R.; Fan, L. S. CO₂ mineral sequestration: Chemically enhanced
532 aqueous carbonation of serpentine. *Can. J. Chem. Eng.* **2003**, *81* (3-4), 885-890.
- 533 23. Gadikota, G.; Park, A.-h. A., Chapter 8 - Accelerated carbonation of Ca- and Mg-bearing
534 minerals and industrial wastes using CO₂. In *Carbon Dioxide Utilisation: Closing the Carbon*
535 *Cycle*, Quadrelli, E. A.; Armstrong, K., Eds. Elsevier: Amsterdam, 2015; pp 115-137.
- 536 24. Gadikota, G.; Swanson, E. J.; Zhao, H.; Park, A.-H. A. Experimental design and data
537 analysis for accurate estimation of reaction kinetics and conversion for carbon mineralization. *Ind.*
538 *Eng. Chem. Res.* **2014**, *53* (16), 6664-6676; 10.1021/ie500393h.
- 539 25. Wilson, S. A.; Barker, S. S. L.; Dipple, G. M.; Atudorei, V. Isotopic disequilibrium during
540 uptake of atmospheric CO₂ into mine process waters: Implications for CO₂ sequestration. *Environ.*
541 *Sci. Technol.* **2010**, *44*, 9522-9529; 10.1021/es1021125.
- 542 26. Wilson, S. A.; Raudsepp, M.; Dipple, G. M. Quantifying carbon fixation in trace minerals
543 from processed kimberlite: A comparative study of quantitative methods using X-ray powder
544 diffraction data with applications to the Diavik Diamond Mine, Northwest Territories, Canada.
545 *Appl. Geochem.* **2009**, *24*, 2312-2331; 10.1016/j.apgeochem.2009.09.018.
- 546 27. Pronost, J.; Beaudoin, G.; Tremblay, J.; Larachi, F.; Duchesne, J.; Hébert, R.; Constantin,
547 M. Carbon sequestration kinetic and storage capacity of ultramafic mining waste. *Environ. Sci.*
548 *Technol.* **2011**, *45*, 9413-9420; dx.doi.org/10.1021/es203063a.
- 549 28. Beinlich, A.; Austrheim, H. In situ sequestration of atmospheric CO₂ at low temperature
550 and surface cracking of serpentinized peridotite in mine shafts. *Chem. Geol.* **2012**, *332-333*, 32-
551 44; <http://dx.doi.org/10.1016/j.chemgeo.2012.09.015>.
- 552 29. Molson, J. W.; Fala, O.; Aubertin, M.; Bussiere, B. Numerical simulations of pyrite
553 oxidation and acid mine drainage in unsaturated waste rock piles. *J. Contam. Hydrol.* **2005**, *78* (4),
554 343-371; 10.1016/j.jconhyd.2005.06.005.
- 555 30. Mavromatis, V.; Pearce, C. R.; Shirokova, L. S.; Bundeleva, I. A.; Pokrovsky, O. S.;
556 Benezeth, P.; Oelkers, E. H. Magnesium isotope fractionation during hydrous magnesium
557 carbonate precipitation with and without cyanobacteria. *Geochim. Cosmochim. Acta* **2012**, *76*,
558 161-174; <http://dx.doi.org/10.1016/j.gca.2011.10.019>.

- 559 31. Shirokova, L. S.; Mavromatis, V.; Bundeleva, I. A.; Pokrovsky, O. S.; Benezeth, P.;
560 Gerard, E.; Pearce, C. R.; Oelkers, E. H. Using Mg isotopes to trace cyanobacterially mediated
561 magnesium carbonate precipitation in alkaline lakes. *Aquat. Geochem.* **2013**, *19* (1), 1-24;
562 10.1007/s10498-012-9174-3.
- 563 32. Power, I. M.; Wilson, S. A.; Thom, J. M.; Dipple, G. M.; Southam, G. Biologically induced
564 mineralization of dypingite by cyanobacteria from an alkaline wetland near Atlin, British
565 Columbia, Canada. *Geochem. Trans.* **2007**, *8* (13).
- 566 33. McCutcheon, J.; Dipple, G. M.; Wilson, S. A.; Southam, G. Production of magnesium-rich
567 solutions by acid leaching of chrysotile: A precursor to field-scale deployment of microbially
568 enabled carbonate mineral precipitation. *Chem. Geol.* **2015**, *413*, 119-131;
569 10.1016/j.chemgeo.2015.08.023.
- 570 34. Thompson, J. B.; Ferris, F. G. Cyanobacterial precipitation of gypsum, calcite, and
571 magnesite from natural alkaline water. *Geology* **1990**, *18*, 995-998.
- 572 35. Schultze-Lam, S.; Fortin, D.; Davis, B. S.; Beveridge, T. J. Mineralization of bacterial
573 surfaces. *Chem. Geol.* **1996**, *132* (1-4), 171-181; 10.1016/s0009-2541(96)00053-8.
- 574 36. Power, I. M.; Wilson, S. A.; Harrison, A. L.; Dipple, G. M.; McCutcheon, J.; Southam, G.;
575 Kenward, P. A. A depositional model for hydromagnesite–magnesite playas near Atlin, British
576 Columbia, Canada. *Sedimentology* **2014**, *61* (6), 1701-1733; 10.1111/sed.12124.
- 577 37. Power, I. M.; Wilson, S. A.; Thom, J. M.; Dipple, G. M.; Gabites, J. E.; Southam, G. The
578 hydromagnesite playas of Atlin, British Columbia, Canada: A biogeochemical model for CO₂
579 sequestration. *Chem. Geol.* **2009**, *260*, 286-300; 10.1016/j.chemgeo.2009.01.012.
- 580 38. Power, I. M.; Harrison, A. L.; Dipple, G. M.; Southam, G. Carbon sequestration via
581 carbonic anhydrase facilitated magnesium carbonate precipitation. *Int. J. Greenhouse Gas Control*
582 **2013**, *16*, 145-155; 10.1016/j.ijggc.2013.03.011.
- 583 39. Peters, K. E.; Walters, C. C.; Moldowan, J. M., *Biomarkers and Isotopes in the*
584 *Environment and Human History*. Cambridge University Press: Cambridge, 2005; Vol. 1, p 1155.
- 585 40. Vonshak, A., Laboratory techniques for the cultivation of microalgae. In *CRC handbook*
586 *of microalgae mass culture*, Richmond, A., Ed. CRC Press Inc.: Boca Raton, 1986; p 117.
- 587 41. McCutcheon, J.; Southam, G. Advanced biofilm staining techniques for TEM and SEM in
588 geomicrobiology: Implications for visualizing EPS architecture, mineral nucleation, and
589 microfossil generation. *Chem. Geol.* **2018**, *498*, 115-127; 10.1016/j.chemgeo.2018.09.016.
- 590 42. McDonald, K., High-pressure freezing for preservation of high resolution fine structure
591 and antigenicity for immunolabeling. In *Electron Microscopy Methods and Protocols*, Nasser
592 Hajibagheri, M. A., Ed. Humana Press: Totowa, NJ, 1999; Vol. 117, pp 77-97.
- 593 43. Parkhurst, D. L.; Appelo, C. A. J. *User's guide to PHREEQC (version 2) - A computer*
594 *program for speciation, batch-reaction, one-dimensional transport and inverse geochemical*
595 *calculations*; U.S. Geological Survey: Denver, 1999; pp 99-4259.
- 596 44. Shuster, J.; Reith, F.; Izawa, M. R. M.; Flemming, R. L.; Banerjee, N. R.; Southam, G.
597 Biogeochemical cycling of silver in acidic, weathering environments. *Minerals* **2017**, *7* (11), 218.
- 598 45. Mook, W.; Bommerso, J.; Staverma, W. Carbon isotope fractionation between dissolved
599 bicarbonate and gaseous carbon-dioxide. *Earth Planet. Sci. Lett.* **1974**, *22* (2), 169-176;
600 10.1016/0012-821x(74)90078-8.
- 601 46. Keeling, C. D.; Piper, S. C.; Bacastow, R. B.; Wahlen, M.; Whorf, T. P.; Heimann, M.;
602 Meijer, H. A., *Exchanges of atmospheric CO₂ and ¹³CO₂ with the terrestrial biosphere and oceans*
603 *from 1978 to 2000*. Scripps Institution of Oceanography: San Diego, 2001; p 88.

- 604 47. Pokrovsky, O. S. Precipitation of calcium and magnesium carbonates from homogeneous
605 supersaturated solutions. *J. Cryst. Growth* **1998**, *186*, 233-239.
- 606 48. Spanos, N.; Koutsoukos, P. G. Kinetics of precipitation of calcium carbonate in alkaline
607 pH at constant supersaturation. Spontaneous and seeded growth. *J. Phys. Chem.* **1998**, *102*, 6679-
608 6684.
- 609 49. Aizenberg, J.; Black, A. J.; Whitesides, G. M. Control of crystal nucleation by patterned
610 self-assembled monolayers. *Nature* **1999**, *398*, 495-498.
- 611 50. Tong, H.; Ma, W.; Wang, L.; Wan, P.; Hu, J.; Cao, L. Control over the crystal phase, shape,
612 size and aggregation of calcium carbonate via a L-aspartic acid inducing process. *Biomaterials*
613 **2004**, *25*, 3923-3929; 10.1016/j.biomaterials.2003.10.038.
- 614 51. Power, I. M.; Kenward, P. A.; Dipple, G. M.; Raudsepp, M. Room temperature magnesite
615 precipitation. *Cryst. Growth Des.* **2017**, *17* (11), 5652–5659; 10.1021/acs.cgd.7b00311.
- 616 52. Markham, G. D.; Glusker, J. P.; Bock, C. W. The arrangement of first- and second-sphere
617 water molecules in divalent magnesium complexes: Results from molecular orbital and density
618 functional theory and from structural crystallography. *The Journal of Physical Chemistry B* **2002**,
619 *106* (19), 5118-5134; 10.1021/jp020078x.
- 620 53. Kluge, S.; Weston, J. Can a hydroxide ligand trigger a change in the coordination number
621 of magnesium ions in biological systems? *Biochemistry* **2005**, *44* (12), 4877-4885;
622 10.1021/bi047454j.
- 623 54. Di Tommaso, D.; de Leeuw, N. H. Structure and dynamics of the hydrated magnesium ion
624 and of the solvated magnesium carbonates: insights from first principles simulations. *Phys. Chem.*
625 *Chem. Phys.* **2010**, *12* (4), 894-901; 10.1039/b915329b.
- 626 55. Slaughter, M.; Hill, R. J. The influence of organic matter in organogenic dolomitization. *J*
627 *Sediment Petrol* **1991**, *61* (2), 296-303.
- 628 56. Wright, D. T.; Wacey, D. Precipitation of dolomite using sulphate-reducing bacteria from
629 the Coorong Region, South Australia: Significance and implications. *Sedimentology* **2005**, *52* (5),
630 987-1008; 10.1111/j.1365-3091.2005.00732.x.
- 631 57. ICDD. International Centre for Diffraction Data. *Magnesite card: 01-071-1534*. **1998**, p 1.
- 632 58. Urmos, J.; Sharma, S. K.; Mackenzie, F. T. Characterization of some biogenic carbonates
633 with Raman spectroscopy. *Am. Mineral.* **1991**, *76* (3-4), 641-646.
- 634 59. Bischoff, W. D.; Sharma, S. K.; MacKenzie, F. T. Carbonate ion disorder in synthetic and
635 biogenic magnesian calcites; a Raman spectral study. *Am. Mineral.* **1985**, *70* (5-6), 581-589.
- 636 60. Wenk, H.-R.; Meisheng, H.; Frisia, S. Partially disordered dolomite; microstructural
637 characterization of Abu Dhabi sabkha carbonates. *Am. Mineral.* **1993**, *78* (7-8), 769-774.
- 638 61. Saldi, G. D.; Jordan, G.; Schott, J.; Oelkers, E. H. Magnesite growth rates as a function of
639 temperature and saturation state. *Geochim. Cosmochim. Acta* **2009**, *73*, 5646-5657;
640 10.1016/j.gca.2009.06.035.
- 641 62. Flemming, H.-C.; Wingender, J. The biofilm matrix. *Nat Rev Micro* **2010**, *8* (9), 623-633.
- 642 63. Körstgens, V.; Flemming, H.-C.; Wingender, J.; Borchard, W. Influence of calcium ions
643 on the mechanical properties of a model biofilm of mucoid *Pseudomonas aeruginosa*. *Water*
644 *Science and Technology* **2001**, *43* (6), 49-57.
- 645 64. Braissant, O.; Decho, A. W.; Przekop, K. M.; Gallagher, K. L.; Glunk, C.; Dupraz, C.;
646 Visscher, P. T. Characteristics and turnover of exopolymeric substances in a hypersaline microbial
647 mat. *FEMS Microbiol. Ecol.* **2009**, *67* (2), 293-307; 10.1111/j.1574-6941.2008.00614.x.
- 648 65. Dupraz, C.; Visscher, P. T. Microbial lithification in marine stromatolites and hypersaline
649 mats. *Trends Microbiol.* **2005**, *13*, 429-438; 10.1016/j.tim.2005.07.008.

- 650 66. Altermann, W.; Kazmierczak, J.; Oren, A.; Wright, D. T. Cyanobacterial calcification and
651 its rock-building potential during 3.5 billion years of Earth history. *Geobiology* **2006**, *4*, 147-166.
- 652 67. Aloisi, G. The calcium carbonate saturation state in cyanobacterial mats throughout Earth's
653 history. *Geochim. Cosmochim. Acta* **2008**, *72*, 6037-6060; 10.1016/j.gca.2008.10.007.
- 654 68. Hänchen, M.; Prigiobbe, V.; Baciocchi, R.; Mazzotti, M. Precipitation in the Mg-carbonate
655 system - effects of temperature and CO₂ pressure. *Chem. Eng. Sci.* **2008**, *63*, 1012-1028;
656 10.1016/j.ces.2007.09.052.
- 657 69. Sánchez-Román, M.; Romanek, C. S.; Fernández-Remolar, D. C.; Sánchez-Navas, A.;
658 McKenzie, J. A.; Pibernat, R. A.; Vasconcelos, C. Aerobic biomineralization of Mg-rich
659 carbonates: Implications for natural environments. *Chem. Geol.* **2011**, *281* (3-4), 143-150;
660 <http://dx.doi.org/10.1016/j.chemgeo.2010.11.020>.
- 661 70. Andres, M. S.; Sumner, D. Y.; Reid, R. P.; Swart, P. K. Isotopic fingerprints of microbial
662 respiration in aragonite from Bahamian stromatolites. *Geology* **2006**, *34* (11), 973-976;
663 10.1130/g22859a.1.
- 664 71. Brady, A. L.; Slater, G. F.; Omelon, C. R.; Southam, G.; Druschel, G.; Andersen, D. T.;
665 Hawes, I.; Laval, B.; Lim, D. S. S. Photosynthetic isotope biosignatures in laminated micro-
666 stromatolitic and non-laminated nodules associated with modern, freshwater microbialites in
667 Pavilion Lake, BC. *Chem. Geol.* **2010**, *274* (1-2), 56-67; 10.1016/j.chemgeo.2010.03.016.
- 668 72. Gibson, J. J.; Edwards, T. W. D.; Bursley, G. G.; Prowse, T. D. Estimating evaporation
669 using stable isotopes - Quantitative results and sensitivity analysis for 2 catchments in northern
670 Canadas. *Nord. Hydrol.* **1993**, *24* (2-3), 79-94.
- 671 73. Lengke, M.; Southam, G. Bioaccumulation of gold by sulfate-reducing bacteria cultured in
672 the presence of gold(I)-thiosulfate complex. *Geochim. Cosmochim. Acta* **2006**, *70* (14), 3646-
673 3661; <http://dx.doi.org/10.1016/j.gca.2006.04.018>.
- 674 74. Trudinger, P. A.; Chambers, L. A.; Smith, J. W. Low-temperature sulphate reduction:
675 Biological versus abiological. *Can J Earth Sci* **1985**, *22* (12), 1910-1918; 10.1139/e85-207.
- 676 75. Revsbech, N. P.; Ward, D. M. Microelectrode studies of interstitial water chemistry and
677 photosynthetic activity in a hot spring microbial mat. *Appl. Environ. Microbiol.* **1984**, *48* (2), 270-
678 5.
- 679 76. Jørgensen, B. B.; Revsbech, N. P.; Blackburn, T. H.; Cohen, Y. Diurnal cycle of oxygen
680 and sulfide microgradients and microbial photosynthesis in a cyanobacterial mat sediment. *Appl.*
681 *Environ. Microbiol.* **1979**, *38* (1), 46-58.
- 682 77. Jørgensen, B. B.; Revsbech, N. P.; Cohen, Y. Photosynthesis and structure of benthic
683 microbial mats: Microelectrode and SEM studies of four cyanobacterial communitie. *Limnol.*
684 *Oceanogr.* **1983**, *28* (6), 1075-1093.
- 685 78. Howsley, R. P., H.W. pH dependent sulfide toxicity to oxygenic photosynthesis in
686 cyanobacteria. *FEMS Microbiol Lett* **2006**, *6*, 287-292.
- 687 79. Schwermer, C. U.; Lavik, G.; Abed, R. M. M.; Dunsmore, B.; Ferdelman, T. G.; Stoodley,
688 P.; Gieseke, A.; de Beer, D. Impact of nitrate on the structure and function of bacterial biofilm
689 communities in pipelines used for injection of seawater into oil fields. *Appl. Environ. Microbiol.*
690 **2008**, *74* (9), 2841-2851; 10.1128/AEM.02027-07.
- 691 80. Joye, S. B.; Paerl, H. W. Nitrogen cycling in microbial mats: Rates and patterns of
692 denitrification and nitrogen fixation. *Mar Biol* **1994**, *119* (2), 285-295; 10.1007/bf00349568.
- 693 81. Harrison, A. L.; Dipple, G. M.; Power, I. M.; Mayer, K. U. Influence of surface passivation
694 and water content on mineral reactions in unsaturated porous media: Implications for brucite

- 695 carbonation and CO₂ sequestration. *Geochim. Cosmochim. Acta* **2015**, *148*, 477-495;
696 <http://dx.doi.org/10.1016/j.gca.2014.10.020>.
- 697 82. McCutcheon, J.; Turvey, C. C.; Wilson, S. A.; Hamilton, J. L.; Southam, G. Experimental
698 deployment of microbial mineral carbonation at an asbestos mine: Potential applications to carbon
699 storage and tailings stabilization. *Minerals* **2017**, *7*, 191.
- 700 83. Hamilton, J. L.; Wilson, S. A.; Morgan, B.; Turvey, C. C.; Paterson, D. J.; MacRae, C.;
701 McCutcheon, J.; Southam, G. Nesquehonite sequesters transition metals and CO₂ during
702 accelerated carbon mineralisation. *Int. J. Greenhouse Gas Control* **2016**, *55*, 73-81;
703 <http://dx.doi.org/10.1016/j.ijggc.2016.11.006>.
- 704 84. Hamilton, J. L.; Wilson, S. A.; Morgan, B.; Turvey, C. C.; Paterson, D. J.; Jowitt, S. M.;
705 McCutcheon, J.; Southam, G. Fate of transition metals during passive carbonation of ultramafic
706 mine tailings via air capture with potential for metal resource recovery. *Int. J. Greenhouse Gas*
707 *Control* **2018**, *71*, 155-167; <https://doi.org/10.1016/j.ijggc.2018.02.008>.
- 708 85. Wilson, S. A.; Harrison, A. L.; Dipple, G. M.; Power, I. M.; Barker, S. L. L.; Ulrich Mayer,
709 K.; Fallon, S. J.; Raudsepp, M.; Southam, G. Offsetting of CO₂ emissions by air capture in mine
710 tailings at the Mount Keith Nickel Mine, Western Australia: Rates, controls and prospects for
711 carbon neutral mining. *Int. J. Greenhouse Gas Control* **2014**, *25*, 121-140;
712 <http://dx.doi.org/10.1016/j.ijggc.2014.04.002>.
- 713 86. Power, I.; McCutcheon, J.; Harrison, A.; Wilson, S.; Dipple, G.; Kelly, S.; Southam, C.;
714 Southam, G. Strategizing carbon-neutral mines: A case for pilot projects. *Minerals* **2014**, *4* (2),
715 399-436.
- 716 87. Power, I. M.; Harrison, A. L.; Dipple, G. M.; Wilson, S. A.; Kelemen, P. B.; Hitch, M.;
717 Southam, G. Carbon mineralization: From natural analogues to engineered systems. *Rev. Mineral.*
718 *Geochem.* **2013**, *77* (1), 305-360; 10.2138/rmg.2013.77.9.
- 719 88. High-Level Commission on Carbon Prices *Report of the high-level commission on carbon*
720 *prices*; Washington, DC, 2017; p 69.
- 721 89. Siegrist, M.; Southam, C.; Bowman, G.; Wilson, S. A.; Southam, G. Analysis of the
722 potential for negative CO₂ emission mine sites through bacteria-mediated carbon mineralisation:
723 Evidence from Australia. *Energy Procedia* **2017**, *114*, 6124-6132;
724 <https://doi.org/10.1016/j.egypro.2017.03.1749>.
- 725 90. Siegrist, M.; Southam, C.; Southam, G. In *An economic analysis of the worldwide potential*
726 *for CO₂ sequestration through bacteria-mediated carbon mineralisation at nickel mine sites*, 30th
727 Australasian Finance and Banking Conference 2017, Sydney, Australia, 2017; Sydney, Australia,
728 2017.
- 729 91. Environment and Climate Change Canada, Technical paper on the federal carbon pricing
730 backstop. In Environment and Climate Change Canada: Gatineau, Canada, 2017; p 22.
- 731 92. IEA, *Energy Technology Perspectives 2017: Catalysing Energy Technology*
732 *Transformations*. Paris, France, 2017.
- 733 93. Mata, T. M.; Martins, A. A.; Caetano, N. S. Microalgae for biodiesel production and other
734 applications: A review. *Renewable and Sustainable Energy Reviews* **2010**, *14*, 217-232.
- 735 94. Ramanan, R.; Kannan, K.; Deshkar, A.; Yadav, R.; Chakrabarti, T. Enhanced algal CO₂
736 sequestration through calcite deposition by *Chlorella* sp. and *Spirulina platensis* in a mini-raceway
737 pond. *Bioresour. Technol.* **2010**, *101*, 2616-2622; 10.1016/j.biortech.2009.10.061.
- 738

